https://doi.org/10.3311/PPci.42490

Periodica Polytechnica Civil Engineering, 70(1), pp. 107–122, 2026

Fragility-based Seismic Assessment of Reinforced Concrete Frame–tube Tall Buildings Incorporating Soil-structure Interaction

Nima Dorrinia[1], Hossein Pahlavan[1*], Mohammad Shamekhi Amiri[1], Mojtaba Sirjani[2]

[1] Faculty of Civil Engineering, Shahrood University of Technology, Haft Tir Square, P.O. Box 3619995161, Shahrood, Iran
[2] College of Science, Engineering and Technology, Norfolk State University, 5115 Hampton Blvd, Norfolk, VA 23529, USA
[*] Corresponding author, e-mail: pahlavan@shahroodut.ac.ir

Received: 13 October 2025, Accepted: 30 December 2025, Published online: 09 February 2026

Abstract

Rapid urbanization and limited available land have increased the construction of high-rise buildings, highlighting the importance of realistic seismic vulnerability assessment in performance-based design. This study analyzes the probabilistic seismic behavior of a 33-story reinforced concrete frame–tube building with core shear walls, modeled according to Iranian seismic codes. Nonlinear Incremental Dynamic Analysis was conducted in MIDAS software under both Fixed Base and Soil–Structure Interaction conditions, using ground motions scaled between 0.1 g and 1.5 g. Fragility curves were generated based on peak inter-story drifts corresponding to four damage states: Slight, Moderate, Extensive, and Complete. Results show that including SSI leads to significantly higher seismic vulnerability, with the structure reaching equivalent damage states at lower PGA levels than the fixed-base model. SSI also causes period elongation and greater deformation demands, indicating the need for enhanced foundation stiffness, soil improvement, or the application of energy-dissipation and isolation strategies to reduce adverse effects. Moreover, comparison of long- and short-period ground motions reveals that the building is more vulnerable to long-period events, especially when SSI is considered. Median PGA thresholds consistently show lower values for SSI across all damage states, confirming the importance of accounting for soil–structure interaction in seismic evaluation. While the results are specific to the soil and structural characteristics studied, the observed trends such as increased seismic demand and vulnerability due to SSI are expected to be applicable to similar high-rise buildings and highlight the need for integrating SSI into future seismic assessments.

Keywords

tall building, soil structure interaction, seismic performance, fragility curve

1 Introduction

The increasing demand for tall buildings stems from population growth, urban constraints, and sustainable development goals. Accurate seismic vulnerability assessment of high-rise buildings is crucial. Although their dynamic response has been studied since the early 2000s, consideration of soil effects is a more recent research area.

Understanding earthquake impacts in dense urban areas helps minimize damage and losses. Fragility and vulnerability curves are essential for seismic risk mitigation, supporting loss forecasting, preparedness, design, insurance, and continuity planning. Due to limited empirical data, these curves are usually developed via analytical or hybrid methods, which are continuously refined [1, 2]. Current discussions also address the impact of uncertainties in these assessments [3]. Extensive research has been conducted on the fragility of buildings, particularly tall structures, underscoring the critical importance of this topic in seismic performance assessment [4–16].

The seismic performance of buildings is influenced by design regulations, typology, and material properties, with the soil–foundation system playing a crucial role due to its nonlinear dynamic behavior affecting seismic response across site conditions [17]. Soil deposits tend to amplify ground motions compared to rock, and soil–structure interaction (SSI) modifies behavior through foundation compliance [18]. Geometric parameters and material nonlinearity also affect the system's response to soil and seismic load severity [19]. While many studies have examined failure patterns in tall reinforced concrete buildings, Gonzalez et al. [20] recently proposed an advanced nonlinear SSI framework for nuclear

Cite this article as: Dorrinia, N., Pahlavan, H., Amiri, M. S., Sirjani, M. "Fragility-based Seismic Assessment of Reinforced Concrete Frame–tube Tall Buildings Incorporating Soil-structure Interaction", Periodica Polytechnica Civil Engineering, 70(1), pp. 107–122, 2026. https://doi.org/10.3311/PPci.42490

facilities. Soil-structure interaction has a significant impact on the behavior of both the structure and the surrounding soil. This influence should be considered not only for specialized structures but also for conventional ones, as their response values may differ substantially from those predicted by decoupled analyses [21]. This study addresses gaps in SSI research for high-rise buildings by developing fragility curves for reinforced concrete (RC) core wall systems that include soil-pile-foundation-structure interactions. Using fragility modifiers (FMs) from the Global Earthquake Model (GEM) framework [22], existing fragility curves are adjusted to incorporate soil nonlinearity and foundation flexibility. The procedure, illustrated in Fig. 1, comprises selecting long and short-period ground motions, modeling a 33-story RC core wall building in Midas [23] with nonlinear finite element analysis, and conducting incremental nonlinear dynamic analysis (IDA) to find floor-specific drifts. These drifts are linked to seismic fragility limit states to evaluate vulnerability and enable improved performance-based seismic design incorporating SSI-aware fragility modifiers.

2 Soil properties

This study highlights the significance of accounting for the nonlinear soil behavior during seismic loading, which motivated the use of the hardening soil model with small-strain stiffness (HSS) for soil characterization, consistent with the approach of [24]. The dynamic soil-structure interaction (SSI) response employing the HSS model was examined by [25]. To evaluate the geotechnical conditions at the site, three boreholes (BH1 to BH3) were drilled to depths of 60 m, with soil samples extracted at various intervals for detailed analysis.

The Standard Penetration Test (SPT) was performed by ASTM D1586 [26], with test spacing decreasing near the surface and increasing at greater depths. After drilling, the SPT sampler was lowered to the target depth, and a 63.5 kg hammer was dropped from 76.2 cm to drive the sampler into the borehole base. This process was repeated across all three boreholes, with the SPT value (N) derived from the blow counts recorded in the final two 15-cm intervals (total 30 cm penetration). This research analyzed soil parameters using the BH3 drilling borehole, with the corresponding SPT chart depicted in Fig. 2. The soil modulus of elasticity (Es) was determined using the shear wave velocity profile and SPT data. The calculations were performed down to a depth of 60 m. To identify soil traits using the HSS model, and m were calculated by correlating Eq. (1) with the shear wave velocity profile. The shear wave velocity profile closely matched the findings from Eq. (1).

$$G_0 = G_0^{ref}\left(\frac{c'\cos\varnothing' + \sigma_3'\sin\varnothing'}{c'\cos\varnothing' + p^{ref}\sin\varnothing'}\right)m \tag{1}$$

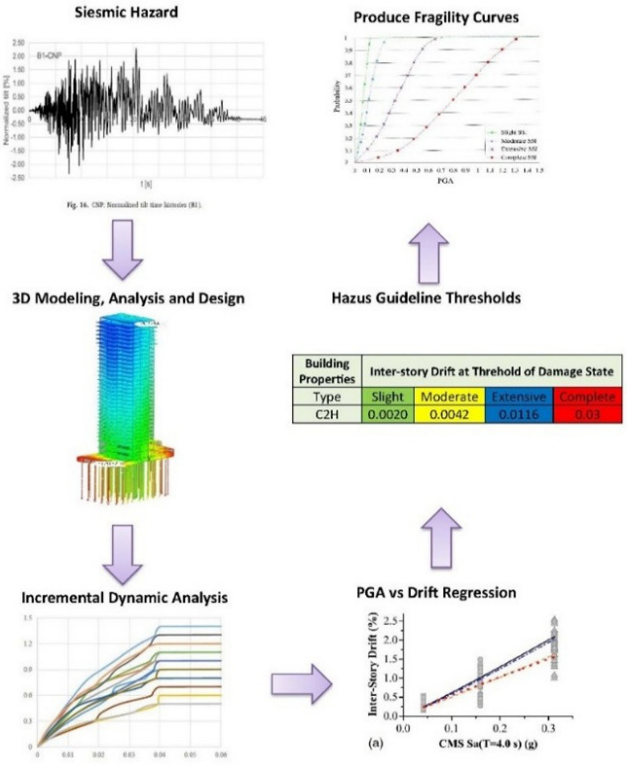

Fig. 1 Procedure of the seismic fragility evaluation considered in the present study

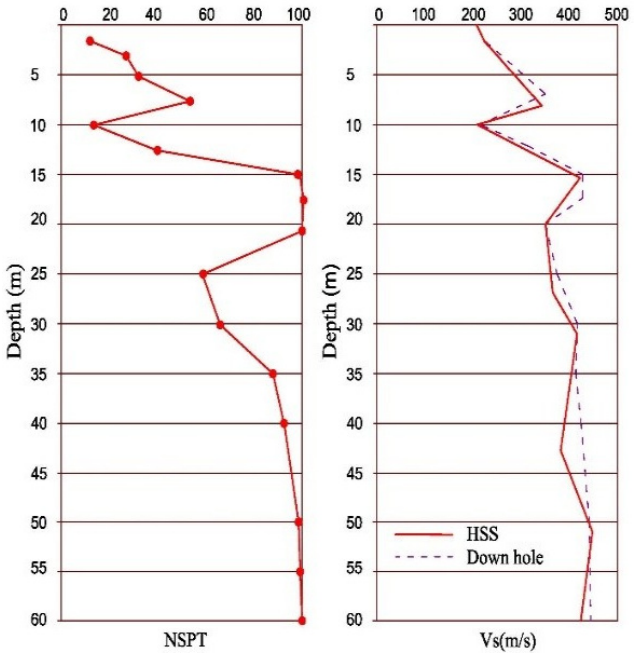

Fig. 2 Site-specific soil profile: shear wave velocity data and the SPT log results

The parameter G_0^{ref} represents the initial shear modulus at the reference confining pressure p^{ref} (taken as 100 kPa). The constant m varies with soil type, and σ'_3 denotes the minor principal effective stress. An essential characteristic of the model is that soil stiffness varies with the stress level, which is incorporated through a function of the effective stress and the strength parameters c' and $\varnothing'$.

Fig. 3 displays data on standard penetration values at various depths, along with information on moisture content (w), relative density (Dr), modified standard penetration values for coarse and fine-grained soils ($N1$ 60, $N1$ 70), wet specific gravity (γ_m), total vertical stress (σ), effective vertical stress (σ'), and soil elastic modulus.

According to the geotechnical report findings and gradation test results, the soil at the site is classified as SP and SP-SM under the Unified Soil Classification System, extending to a depth of 10 m. At depths between 10 and 12.5 m, the soil transitions to fine-grained material classified in the ML category. From 12.5 to 60 m, the soil is predominantly classified as SP and SM. This study incorporated three representative soil layers corresponding to the BH3 borehole test and their respective properties into the MIDAS software model [23], as detailed in Table 1. A schematic illustration of the soil strata and the structural configuration as modeled in MIDAS [23] is presented in Fig. 4.

3 Numerical modeling

This study analyzed a 33-story reinforced concrete core frame building in Babolsar, Iran, using two numerical models in MIDAS GTS NX [23]. The first assumed a fixed-base supported by piles, while the second included soil-structure interaction (SSI) by modeling soil, foundation, and structure together to capture their complex seismic response. MIDAS GTS NX [23] was chosen for its advanced ability to simulate coupled soil-structure behavior, enabling realistic assessment of soil flexibility, damping, and energy dissipation effects. Comparing the fixed-base and SSI models emphasizes the important influence of soil-structure interaction on the seismic performance of tall buildings in this area.

4 Structural specifications

The analyzed structure is a 33-story residential high-rise with a core-frame system, totaling 116 m in height (first floor 4 m, subsequent floors 3.5 m). Beams and columns are modeled as frame elements, excluding longitudinal reinforcement slip in plastic hinge zones, a simplification common in seismic design codes [27]. The same modeling assumptions were applied for fixed-base and soil-structure interaction (SSI) analyses to clearly assess SSI effects. The building features a 0.3 m thick waffle concrete slab, live load of 200 kg/m^2, and dead load of 160 kg/m^2 on floors. Deep piles and a mat foundation (30 × 46 m, 4 m deep) with appropriate stiffness are essential for load distribution. Allowable soil pressures are 4.2 kg/cm^2 (gravity) and 5.6 kg/cm^2 (seismic), while actual pressures are below these limits. However, mat foundation settlement alone exceeds allowable limits by about 40 cm, justifying the combined mat and pile foundation modeled in MIDAS [23]. The floor plan is shown in Fig. 5, and column and beam sizes are detailed in Table 2.

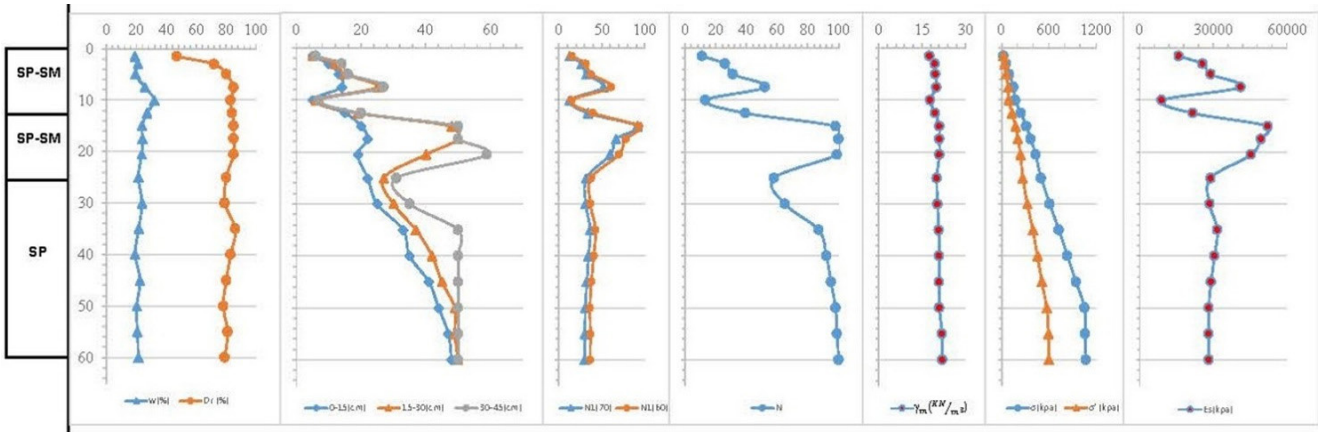

Fig. 3 Condensed subsurface conditions relevant to Babolsar city

Table 1 Soil parameters input into the MIDAS software

Soil Type	Depth	γ (kg/m^3)	Dr (%)	$\varnothing$	Es (kg/cm^2)
SP-SM	0–12	1900	71	35	160
SP-SM	12–24	2000	85	37	450
SP	24–60	2100	81	40	920

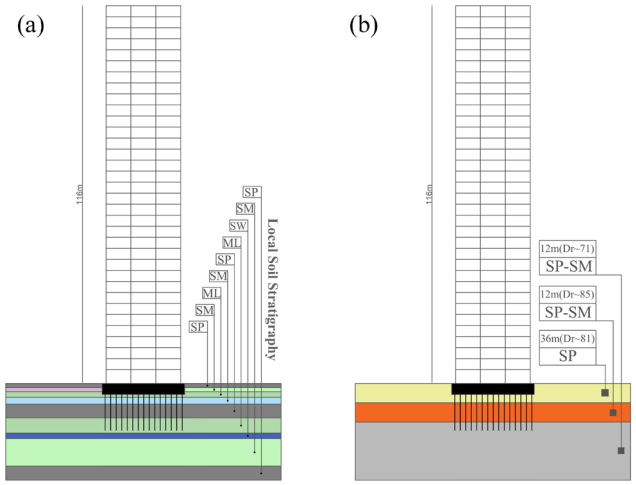

Fig. 4 Diagram of the model including structure, foundation, pile, and soil: (a) Local soil stratigraphy, (b) Soil profile modeled in MIDAS

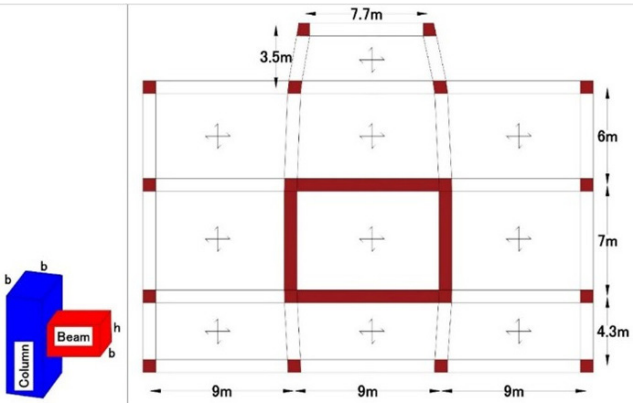

Fig. 5 Layout illustration of beams and columns

Table 2 Columns and beams geometric measurements

Story No.	Columns ($b \times b$) (cm)	Beams ($b \times h$) (cm)
1–9	95 × 95	95 × 65
10–18	90 × 90	90 × 60
19–33	80 × 80	80 × 60

Ductility in moment-resisting frames is provided by the beams' flexural capacity. Materials that exhibit ductile characteristics can endure plastic deformation without experiencing a notable decrease in strength. Furthermore, these components possess the ability to absorb the energy from seismic activity due to their adaptable nature. The nonlinear response of the structure was modeled by incorporating plastic hinges at the beam ends, following the methodology proposed by [28, 29]. Fig. 6 presents the moment-curvature relationship, visually depicting the behavior of the plastic hinge. Flexural stiffness (EI) at the beam ends and the plastic moment ($M_n = M_p$) were calculated using Eqs. (2)–(4):

$$E_c I_{eff} = 0.3 E_c I_g \text{ for beams} \tag{2}$$

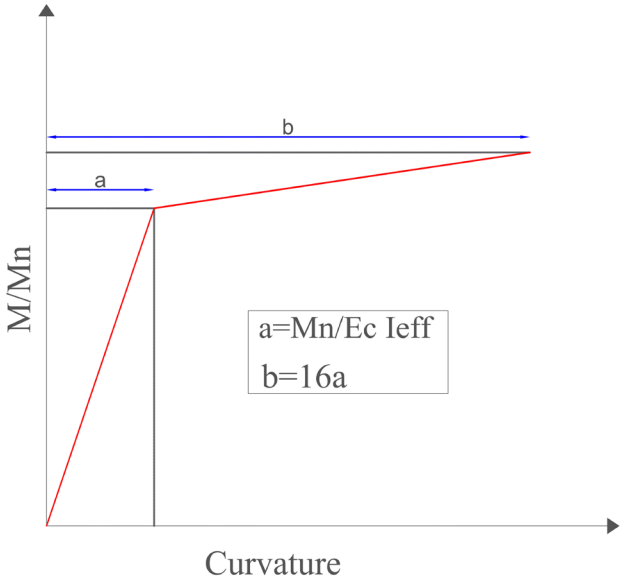

Fig. 6 Bilinear moment-curvature curve for the plastic hinge

$$E_c I_{eff} = \frac{M_n}{2\varepsilon_y} \text{ for columns} \tag{3}$$

$$M_n = M_p = A\sigma_y y_g \tag{4}$$

where E_c represents the elastic modulus of concrete, I_g is the gross moment of inertia, y_g the distance between the centroid of tensioned or compressed zones of cross-section and neutral axis, A represents the area of the cross-section, ε_y denotes the yield strain of steel reinforcement, and σ_y is the compressive strength of concrete.

MIDAS software [23] incorporates the cracking coefficient for both beams and columns within its nonlinear analysis framework, aligning with the requirements set forth by performance-based seismic design guidelines (TBI). This integration allows for more accurate simulation of the structural behavior under seismic loading by considering the stiffness reduction due to cracking in reinforced concrete elements. The specific values and implementation details of these cracking coefficients are comprehensively summarized in Table 3, providing essential parameters that enhance the fidelity of seismic performance assessments using MIDAS [23]. This feature supports engineers in achieving more reliable and code-compliant structural designs under earthquake conditions.

Table 3 Cracking coefficient in beams and columns

Level nonlinear model			
Component	Axial	Flexural	Shear
Beams	1.0EcAg	0.3EcIg	0.4EcAg
Columns	1.0EcAg	0.7EcIg	0.4EcAg

The primary structural component of the building is a box-shaped wall with openings on the north and south sides, included according to design requirements. This wall spans from the foundation to the 33rd floor. Detailed specifications of the coupled shear wall components are provided in Table 4, and its design and dimensions are illustrated in Fig. 7.

5 Pile loading test (verification 1)

Four piles in the structure were statically load tested, with two tests verified using MIDAS software [23]. Incremental axial loads were applied using a hydraulic jack with a calibrated pressure gauge, while pile head deformation was measured by displacement transducers. Testing followed ASTM D1143-07 [30] and project specifications. Piles were loaded to maximum capacities between 750 and 900 t and then unloaded to assess elastic recovery. Vertical displacements were continuously recorded during loading and unloading. Fig. 8. shows the test setup, instrumentation, and load application.

The load-displacement diagrams in Fig. 9 show the bearing capacity results of all four test piles. Additionally, Fig. 10 displays the assessed design of the presents model of the structure piles with a mat foundation, in MIDAS software [23].

Various pile load testing methods depend on factors like pile properties, soil type, testing method, pile-soil interaction, displacement, curve gradient, and soil deformation. Table 5 presents results from four methods, emphasizing Davison's and Butler and Hoy's for maximum load. Typically, allowable pile load equals ultimate capacity divided by a safety factor, The safety factor for the allowable pile load was reduced from the typical value of 2.5 to 2.2 because the tests were conducted under final conditions, where the pile behavior closely reflects the actual site conditions. Under such circumstances, it is justified to adopt a slightly lower safety factor [31]. Here, the "actual conditions" refer to four piles considered under the site-specific conditions, with consistent soil properties and static loading corresponding to those piles. Furthermore, the settlement results of two of these four piles were verified against the predictive model, providing additional confidence in the reduced safety factor. Table 5 summarizes settlements at failure loads with this factor and compares allowable loads. Test piles showed: PT-1 (25 m) settlement of 70 mm at 910 t load and 63 mm post-unloading; PT-2 (30 m) 100 mm at 796 t and 99 mm after unloading; PT-3 (25 m) over 50 mm at 765 t and 42 mm post-unloading; PT-4 (30 m) 61 mm at 863 t and 46 mm after unloading. Settlements for PT-1 and PT-2 were numerically analyzed in MIDAS [23] with loading at multiple points from load diagrams (Fig. 11), showing less than 10% deviation from test data. MIDAS [23] predicted 65 mm settlement for PT-1 at 900 t and 100 mm for PT-2 at 800 t, confirming accurate modeling. Nine load points per pile were applied, matching static load tests closely, demonstrating the precision of the modeling approach and MIDAS software [23] effectiveness. Loads applied via MIDAS's Assign Load function for PT-1 were 150 to 900 t at various steps, and for PT-2, 100 to 800 t incrementally.

6 Verification 2

To further ensure the reliability and reproducibility of the proposed numerical model in MIDAS GTS NX [23], a second independent verification was performed using the well-documented shear wall experiment conducted by [32]. This specimen was deliberately selected because it represents a flexure-dominated reinforced concrete wall with well-defined boundary element confinement a structural typology very similar to the pile-supported walls investigated in the present study. Fig. 12 illustrates the overall shape and dimensions of the walls that were tested. The tested wall had a height of 3.66 m, thickness of 0.10 m, and length of 1.22 m. The concrete compressive strength was fc' = 27.4 MPa and the modulus of elasticity was taken as Ec = 24,800 MPa. Longitudinal reinforcement consisted of 8 #3 bars (∅9.5 mm) yielding fy = 414 MPa, while transverse reinforcement in the confined boundary zones comprised ∅4.8 mm closed hoops and crossties at 76 mm spacing (s = 8 db). The axial load ratio was approximately $0.07fc'Ag$. The wall model in MIDAS [23] utilized 2D plate elements with layered nonlinear material properties. Concrete was modeled using the Mander et al. (1988) [33] confined concrete model with the following calibrated parameters:

- Unconfined concrete strength fco = 27.6 MPa
- Confined concrete strength fcc = 34.2 MPa (calculated from measured hoop spacing and yield strength)

Table 4 The core frame system details

Story No.	Wall width	Opening 1 and 2	Horizontal rebar	Upright rebar	Column measurements
1–9	0.70 m	2.2 m × 2.4 m	∅ 20 @ 20	∅ 22 @ 20	0.9 m × 0.70 m
10–20	0.65 m	2.2 m × 2.4 m	∅ 18 @ 20	∅ 22@ 25	0.8 m × 0.70 m
21–29	0.60 m	2.2 m × 2.4 m	∅ 16 @ 20	∅ 20 @ 25	0.8 m × 0.65 m
30–33	0.55 m	2.2 m × 2.4 m	∅ 16 @ 25	∅ 20 @ 25	0.8 m × 0.65 m

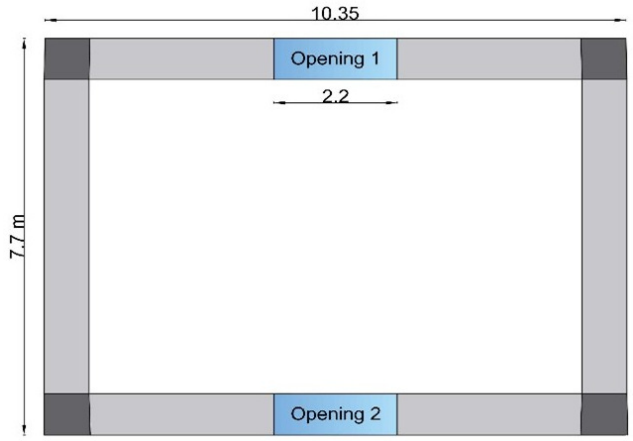

Fig. 7 Wall design and dimensions (Core Tube Frame)

Fig. 8 Field implementation of the Pile Load Test conducted in this study

- Strain at peak unconfined strength $\varepsilon co = 0.002$
- Ultimate confined strain $\varepsilon cu = 0.012$ (based on confinement ratio $\rho s = 0.0127$ and $fyh = 490$ MPa).

Reinforcing steel was modeled using a bilinear kinematic hardening rule with $fy = 490$ MPa, ultimate strength $fu = 686$ MPa, and hardening ratio of 1%. Effective cracked moment of inertia was taken as $Ie = 0.35Ig$ for service load levels and further reduced to $0.25Ig$ in the plastic hinge region following calibration. Lateral loading followed the displacement-controlled reversed cyclic protocol identical to the original experiment. Model calibration was performed iteratively by adjusting the concrete tensile strength ($ft = 2.8$ MPa) and interface shear stiffness until the initial stiffness, yield point, peak lateral strength ($V_{peak,exp} = 92.5$ kN vs. $V_{peak,num} = 94.1$ kN, error 1.7%), and energy dissipation per cycle matched the experimental results within ±5%. Fig. 13 presents the comparison between the experimental and numerical hysteresis loops. Despite differences in material parameters between MIDAS [23] and lab conditions, the simulation effectively captured nonlinear frame behavior,

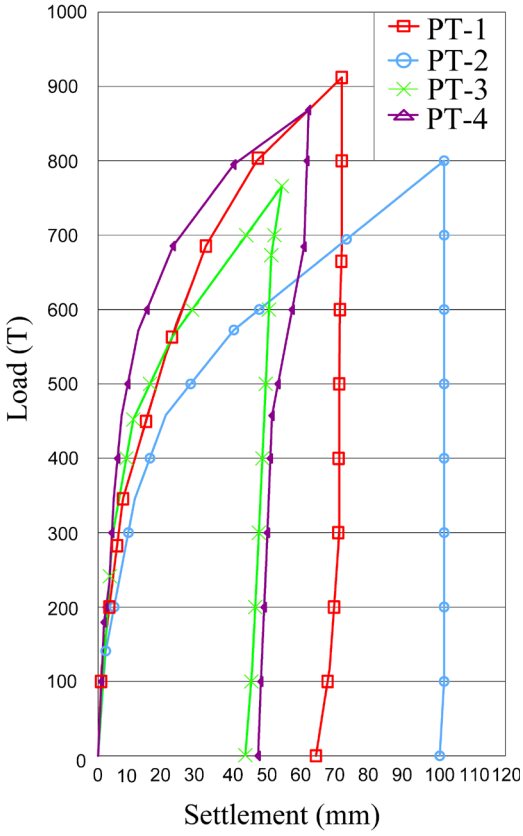

Fig. 9 The settlement versus load curves for the four different pile tests conducted

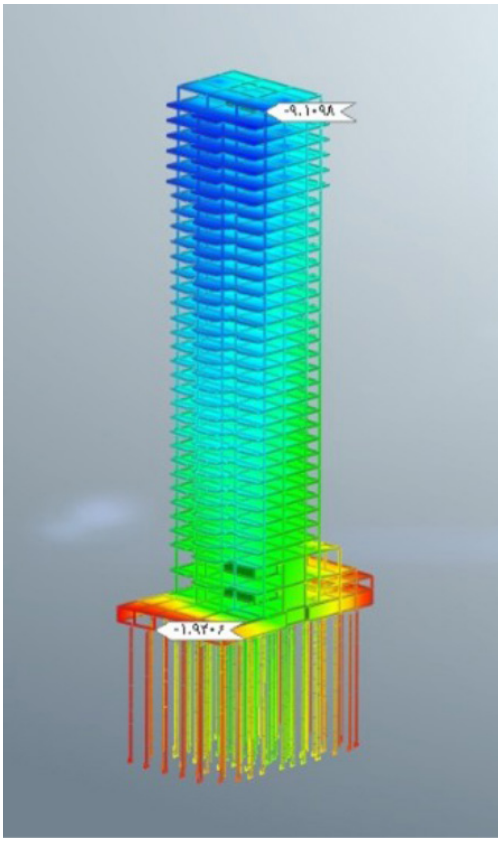

Fig. 10 Structure modeling with foundation and pile in the MIDAS

Table 5 Measured settlement and load parameters for the four tested piles

Pile name	Pile specifications		Failure load base on interpolation methods (t)					Proposed ultimate load (t)	Corresponding settlement (mm)	Alloawbale capacity (t) SF = 2.2
	Length (m)	Diameter (cm)	Butler & Hoy	2 - Line	Davison	Chin-Kondner	Brinch-Hansen			
PT – 1	25	100	880	640	560	-	-	690	36	345
PT – 2	30	100	760	500	520	-	-	640	46	290
PT – 3	25	100	720	500	550	909	884	635	31	288
PT – 4	30	100	820	700	680	1000	837	750	32	340
	Average 25 m		800	545	555	909	884	662	-	300
	Average 30 m		790	590	580	1000	837	695	-	315

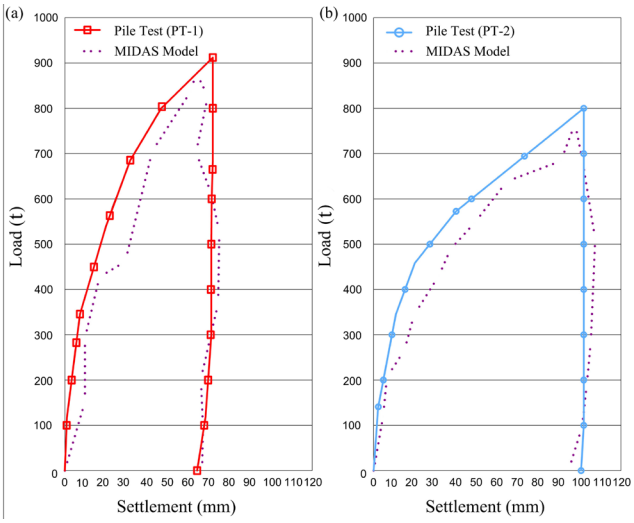

Fig. 11 The outcomes of the tested piles and the results obtained from the MIDAS model

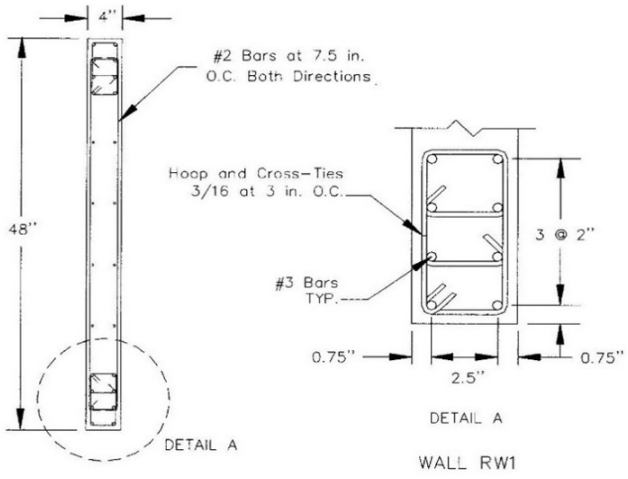

Fig. 12 Dimensions and specifications of the shear wall studied for validation [32]

showing strong agreement with experiments, especially in peak displacements, with minimal discrepancies.

7 Boundary conditions and interface characteristics

Boundary conditions and interface characteristics are essential factors that must be carefully evaluated to ensure the accuracy and reliability of numerical simulations. It is crucial

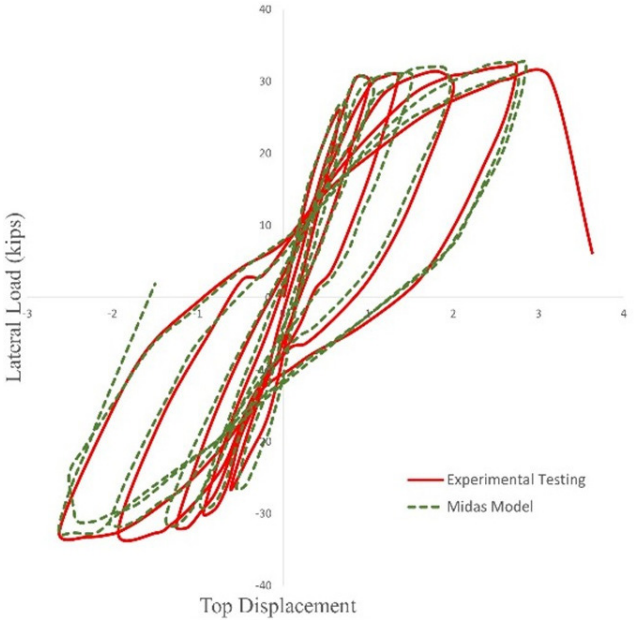

Fig. 13 The Hysteresis curve obtained from the experimental test of a shear wall and its modeling in Midas

to select boundary conditions that prevent the exclusion of high-frequency components of the input excitations, which otherwise may lead to inaccurate representation of the dynamic response. Consequently, element sizes in the model are typically determined based on the highest input excitation frequencies and the soil's shear wave velocity. Specifically, the element dimensions are chosen to be between one-fifth and one-eighth of the corresponding wavelength of the initial excitation, multiplied by a factor as suggested by [34], to adequately capture the wave propagation effects.

This study used an infinite boundary condition with a free-field approach to simulate the surrounding soil extending infinitely, minimizing artificial wave reflections and replicating realistic wave propagation. The model's lateral soil boundaries were connected to the open environment via viscous dampers that absorb outgoing waves, with damping coefficients calculated automatically in MIDAS GTS NX [23] based on P- and S-wave velocities. The bedrock was modeled with rigid boundary conditions

to simulate accurate soil-structure interaction (SSI) and two-way SSI effects. Input motion was applied directly at the base nodes, following [35].

Accurate modeling of the interface behavior between the foundation and adjacent soil is critical due to the complex interaction mechanisms. To represent this, a strength reduction factor, denoted as , was introduced within the Mohr-Coulomb failure criterion. This factor accounts for the potential reduction in shear strength along the interface and is incorporated through the following governing Eqs (5–7), which describe the mechanical behavior at the soil-foundation interface. This approach enhances the realism of the simulation by capturing slip and separation phenomena that could significantly influence overall structural response.

$$R_{\text{inter}} \times \left(K_n u_n + K_t u_t \tan(\varnothing) - C\right) = 0 \tag{5}$$

$$K_n = \frac{E_{oed.i}}{\sqrt{A' t_v}} \tag{6}$$

$$K_t = \frac{R_{\text{inter}} G_{ur}}{\sqrt{A' t_v}} \tag{7}$$

In these Eq, u_n and u_t refer to the relative vertical and horizontal displacements at the interfaces. The interface area between the soil and foundation is denoted as A', while t_v represents the interface's virtual thickness, set at 0.1 as advised by [36]. $E_{oed.i}$ indicates the interface oedometer modulus, G_{ur} is the average unloading-reloading shear modulus, K_t and K_n represent the interface stiffness. Using these expressions, the interface between the two components was modeled with normal and shear linear springs. The actual interface strength depends on factors like material type (e.g., soil, concrete) and foundation area, typically ranging between 0.12 and 1. Based on previous studies by [37, 38] on soil-foundation interfaces, the parameter R_{inter} was set to 0.75 in this study.

8 Earthquake ground motion data

In nonlinear dynamic analysis, accuracy depends on selecting ground motion records that represent the Maximum Considered Earthquake (MCE) hazard level per FEMA P695 [39] and ASCE 7-10 [40]. These accelerograms must suit three-directional time history analysis and capture structural response from elastic to collapse stages, often evaluated via Incremental Dynamic Analysis (IDA). Records should also match the site's soil type, with a minimum of 22 records recommended for statistical reliability. Following FEMA P695 [39] guidelines is essential for robust assessment of structural vulnerability and collapse risk under severe earthquakes.

This study utilizes ground motion records as specified by the FEMA P695 [39] guidelines. corresponding to the same soil type as the construction site, were selected and analyzed using SeismoSignal software.[41]. Based on their frequency domain spectra and average period and frequency characteristics, the accelerograms were classified into two categories: long-period and short-period records. Due to the limited number of available long-period records in the FEMA P695 [39] set, an additional 22 accelerograms were sourced from the PEER earthquake database for Incremental Dynamic Analysis (IDA), selected according to the FEMA P695 [39] criteria. All records were matched to the construction site soil type and analyzed individually using Seism Signal. The Fourier spectrum was utilized as the primary tool to assess the frequency content of each accelerogram accurately. Classification into long-period or short-period categories was based on the Fourier spectrum characteristics and the computed mean period. This means period, a key parameter for classification, was determined using Eq. (8).

$$T_m = \frac{\sum_i C_i^2 \left(\frac{1}{f_i}\right)}{\sum_i C_i^2} \tag{8}$$

The mean period T_m, is calculated from the Fourier spectrum C_i of the accelerogram, where f_i represents the discrete frequencies obtained via the Fourier transform. An accelerogram is classified as a long-period record if its average Fourier amplitude period exceeds 1 s and its peak amplitude is found at a frequency lower than 1 Hz, as depicted in Fig. 14 (b). Conversely, for short-period accelerograms, the mean period associated with the peak Fourier amplitude is less than 1 second, and the maximum amplitude appears at frequencies higher than 1 Hz, as shown in Fig. 14 (a). Following FEMA P695 [37], ground motion records are divided into short-period and long-period sets detailed in Tables 6 and 7, respectively.

Also, Fig. 15 illustrates the resulting short- and long-period design spectra derived from the scaled accelerograms. Modal analysis validated the building model's accuracy, stability, and fundamental periods, guiding ground motion selection and scaling. Structures with soil-structure interaction (SSI) show longer fundamental periods compared to fixed-base models due to soil deformation effects. Table 8 and Fig. 16 show that fixed-base periods are about 74% (first mode) and 70% (second mode) of SSI periods. This increased flexibility under SSI affects seismic energy dissipation. Beyond the third mode, periods decrease as soil influence lessens, with higher modes approaching

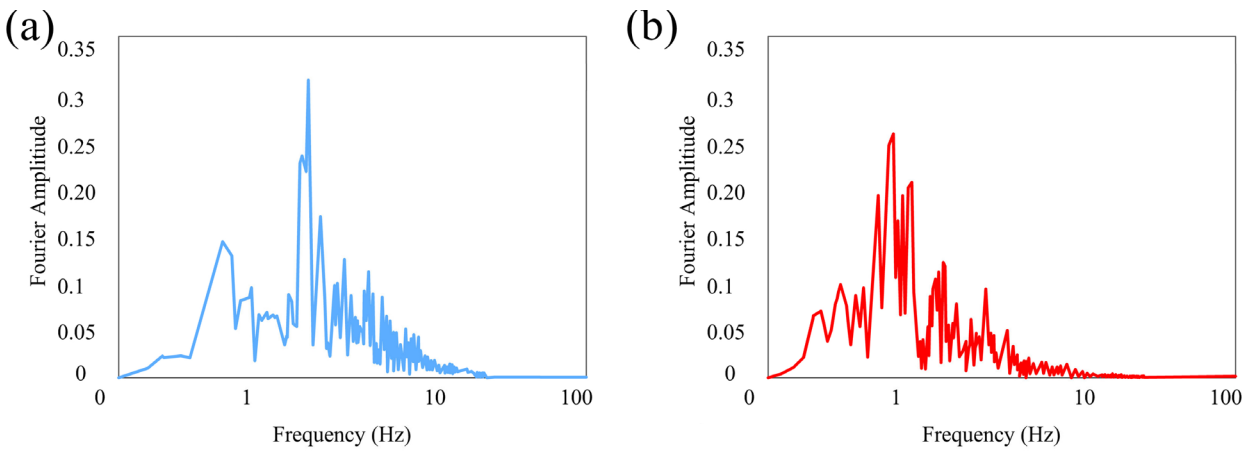

Fig. 14 Fourier amplitude spectrum of (a) a short-period accelerogram with a mean period of 0.59 s and (b) a long-period accelerogram with a mean period of 1.24 s

Table 6 The records categorized into accelerometers with Short Period

NO	Earthquake			Station Name	Direction	Period Time (s)
	Magnitude	Year	Record Name			
1	6.9	1995	Kope, Japan	Shin-Osaka	SHI000	0.75
2	7.3	1992	Landers	Cool water	LN	0.42
3	6.9	1989	Loma Prieta	Capitola	CAP000	0.49
4	6.9	1989	Loma prieta	Gilroy Array #3	G03000	0.37
5	6.5	1987	Superstition Hills	Poe Road (temp)	POE270	0.48
6	7.0	1992	Cape Mendocino	Rio Dell Overpass	RIO360	0.44
7	6.6	1971	San Fernando	LA – Hollywood	PEL180	0.35
8	6.5	1979	Imperial Valley	Chihuahua	CHI012	0.57
9	6.5	1979	Imperial Valley	Bonds Corner	BCR140	0.48
10	6.7	1994	Northridge-01	Northridge - Saticoy	STC090	0.6
11	6.7	1994	Northridge-01	Rinaldi Receiving Sta	RRS228	0.76

Table 7 The records categorized into accelerometers with Long Period

NO	Earthquake			Station Name	Direction	Period Time (s)
	Magnitude	Year	Record Name			
1	6.7	1992	Erzican, Turkey	Erzincan	ERZ-NS	1.38
2	7.6	1999	Chi-Chi, Taiwan	TCU065	E	1.129
3	6.3	1992	Landers	Anaheim - W Ball Rd	WBA00	1.16
4	6.5	1954	Northern Calif-03	Ferndale City Hall	FRN044	1.24
5	6.3	1992	Landers	Buena Park	BPK090	1.26
6	6.5	1979	Imperial Valley	El Centro	EMO270	1.78
7	6.3	1980	Imperial Valley	Chihuahua	CHI192	1.09
8	6.3	1992	Landers	Inglewood - Union	ING000	1.25
9	6.6	1968	Borrego Mtn	El Centro Array #9	ELC180	1.33
10	6.3	1992	Landers	Downey	DWN000	1.25
11	6.3	1980	Victoria_ Mexico	Victoria Hospital	HPB000	1.02

fixed-base behavior. Including SSI in dynamic analysis is crucial for realistic seismic performance assessment, addressing the interaction between soil and structure [42].

9 Introduction of hazard levels

The HAZUS MHMR5 framework divides seismic hazard into four levels: low, medium, high, and complete, facilitating systematic vulnerability assessment. Table 9 shows

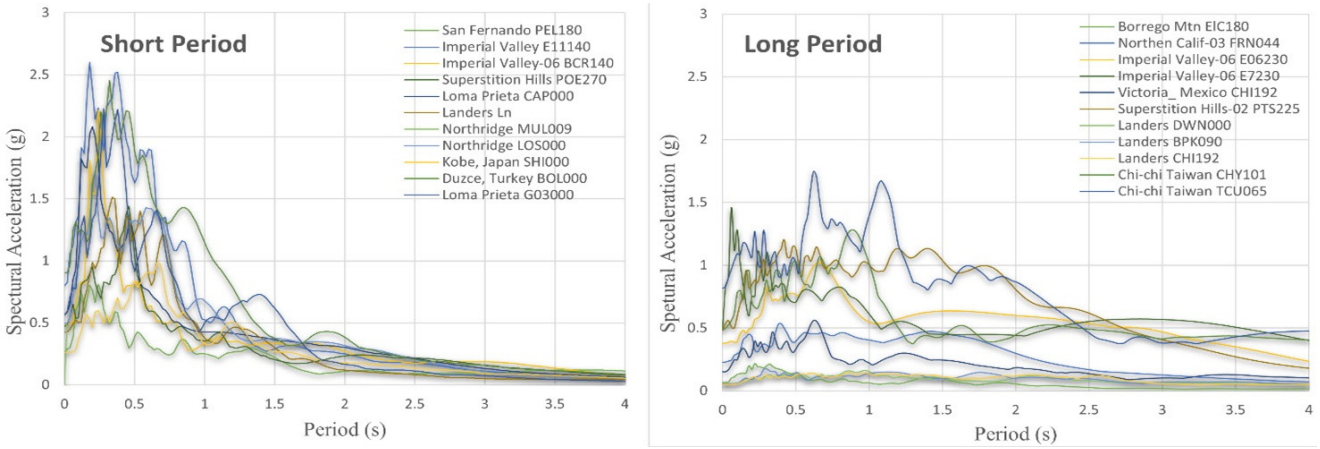

Fig. 15 Short-period and long-period design spectra of the scaled accelerograms

Table 8 The first ten modes for two models: Fixed Base and SSI

	Fixed Base					SSI				
Mode	Period (s)	UX	UY	SumUX	SumUY	Period (s)	UX	UY	SumUX	SumUY
1	3.015	0.0006	0.5739	0.0006	0.5739	4.084	0.6148	0.0002	0.6148	0.0002
2	2.657	0.5751	0.0006	0.5757	0.5745	3.784	0.0002	0.5813	0.615	0.5815
3	1.104	4.75E-05	3.13E-06	0.5758	0.5745	1.126	1.61E-05	3.8E-06	0.615	0.5815
4	0.669	0.0001	0.1818	0.5759	0.7563	0.744	0.0003	0.1581	0.6153	0.7397
5	0.572	0.1921	0.0001	0.768	0.7564	0.683	0.1517	0.0003	0.7671	0.74
6	0.395	0.0043	1.85E-05	0.7723	0.7564	0.404	0.0016	1.78E-05	0.7687	0.74
7	0.287	0.0003	0.0668	0.7726	0.8232	0.31	0.0001	0.0555	0.7689	0.7955
8	0.263	0.0387	0.0008	0.8113	0.824	0.28	0.0359	0.0003	0.8048	0.7959
9	0.218	0.0395	4.78E-05	0.8508	0.8241	0.231	0.017	0.0001	0.8217	0.7959
10	0.18	0.007	0.0018	0.8579	0.8258	0.184	0.0038	0.0039	0.8256	0.7999

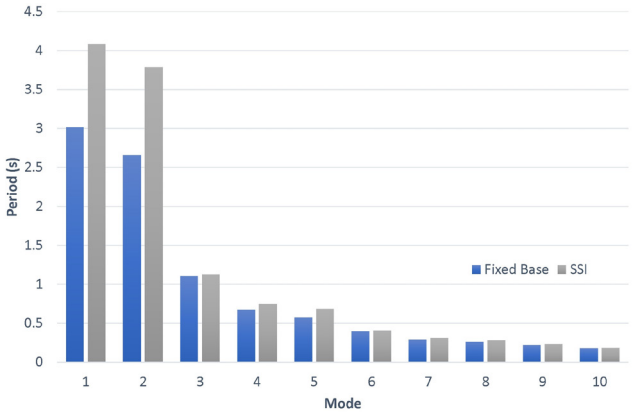

Fig. 16 Period value in each mode for Fixed Base and SSI model

Table 9 Parameters of structural fragility curves under moderate seismic code provisions

Building Properties	Inter-story Drift at Threhold of Damage State			
Type	Slight	Moderate	Extensive	Complete
C2H	0.0020	0.0042	0.0116	0.03

maximum relative floor displacements for tall buildings with specialized concrete across damage states, from slight damage to total failure. These displacement values are key for defining mid-range relative displacement capacity, essential for developing precise fragility functions. Incorporating these thresholds improves the accuracy of seismic risk assessments for high-rise concrete buildings.

10 Incremental Dynamic Analysis (IDA)

A detailed 33-story high-rise model was developed in Midas [23] and analyzed using Incremental Dynamic Analysis (IDA) for seismic performance assessment [43]. IDA systematically scales ground motions to evaluate building behavior from elastic to collapse states, assessing structural capacity and damage probabilities. Nonlinear material properties were included for realistic simulations. Two sets of ground motions were used: short-period records analyzed with 0.1 g scaling increments up to 1.5 g, and long-period records with finer 0.05 g increments due to higher response sensitivity [44]. Fragility curves generated from these analyses are shown in Figs. 17 and 18 for fixed-base and SSI models, illustrating maximum inter-story drifts under short- and long-period motions. Short-period

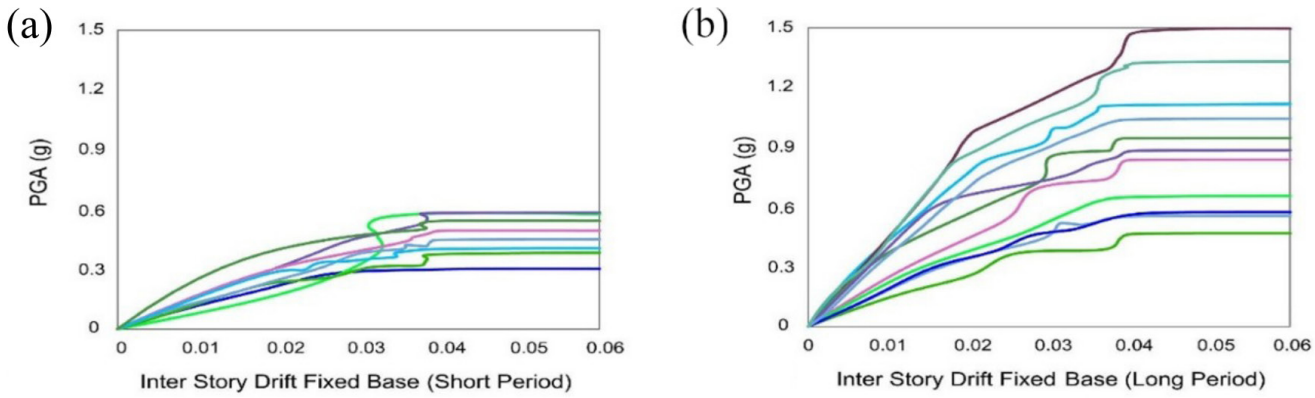

Fig. 17 The IDA curves for Fixed Base Model, (a) Short Period earthquake and (b) Long Period earthquake

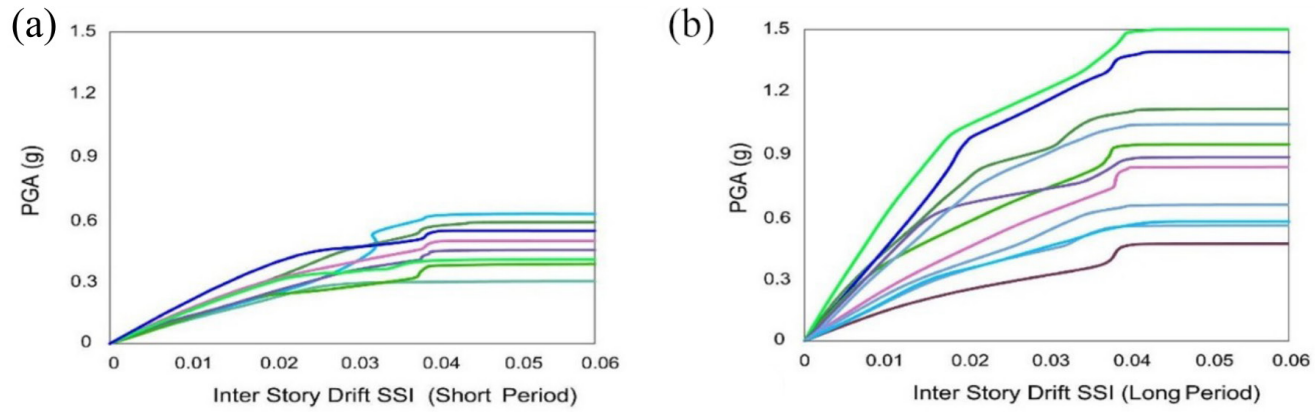

Fig. 18 The IDA curves for SSI Model, (a) Short Period earthquake and (b) Long Period earthquake

curves plateau at lower PGAs, indicating early drift limits, while long-period curves rise steeply, showing increased vulnerability to large drifts with higher seismic intensity, highlighting the importance of considering spectral content in tall building seismic evaluations [45].

11 Seismic fragility curves

Fragility curves offer a probabilistic method to assess the likelihood of a structure exceeding specific damage states based on seismic response, influenced by each building's unique traits. They predict building performance under earthquake loads. To develop fragility curves from engineering demand parameters obtained via Incremental Dynamic Analysis (IDA), an assumed probability distribution is needed. This study uses the log- normal distribution, justified by the central limit theorem, which approximates combined structural response when both capacities and seismic demands follow normal distributions. The fragility curves are thus formulated using Eq. (9).

$$P(c \le D) = \varnothing\left(\frac{\ln\left(S_d / S_c\right)}{\beta_{sd}}\right) \tag{9}$$

In the relationship mentioned above, P denotes the cumulative probability of exceeding the specified engineering demand parameter, which in this research refers to the highest non-linear drift in layers. β_{sd} denotes the standard deviation of the logarithm of the standard demand parameter, *cs* is the median capacity value at various damage levels sourced from Table 9, and *ds* also represents the median demand parameter for earthquakes, specifically the maximum nonlinear drift obtained from the analyses.

Fragility curves in Fig. 19 show that the fixed-base structural model is more vulnerable to long-period ground motions than short-period ones. Fig. 19 (a) illustrates a gradual increase in the probability of extensive and complete damage with rising PGA for short-period motions, indicating a slower damage progression. In contrast, Fig. 19 (b) reveals a rapid rise in damage probabilities at lower PGA values for long-period motions, highlighting greater vulnerability and higher chances of severe damage under long-period seismic loading.

Fig. 20 shows that fragility curves from the soil-structure interaction (SSI) model reveal greater structural vulnerability to long-period ground motions than short-period motions across all risk levels. This emphasizes the significant impact of dynamic SSI effects on seismic performance, especially for low-frequency earthquakes. The results suggest that design and mitigation efforts should focus on long-period

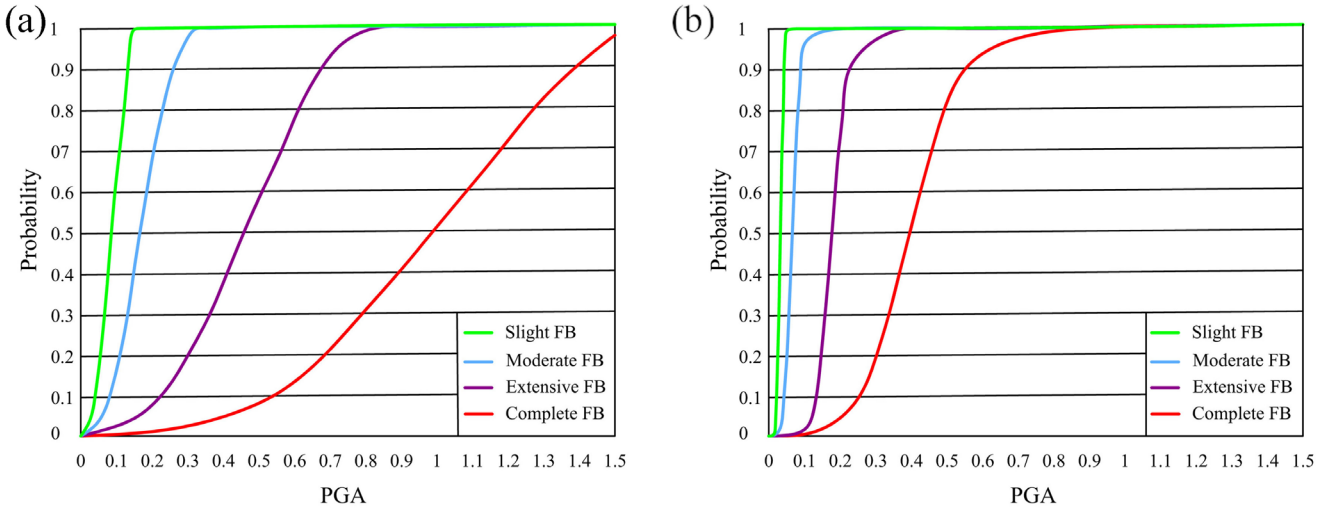

Fig. 19 The fragility curves at various damage states for a fixed-base model under (a) Short period earthquake and (b) Long period earthquake

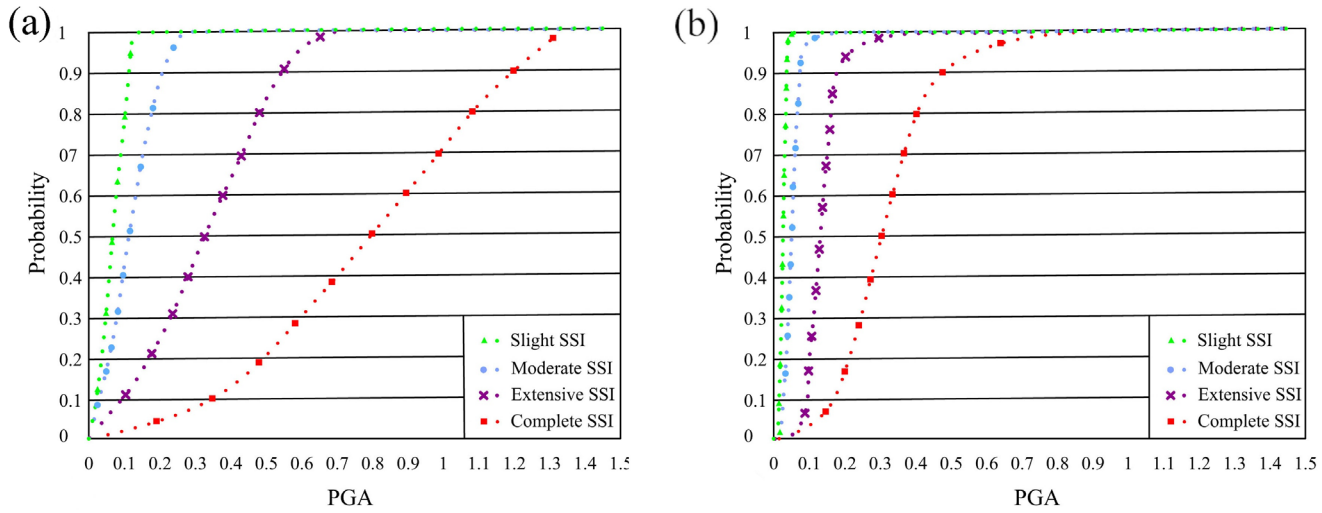

Fig. 20 The fragility curves at various damage states for SSI model under (a) Short period earthquake and (b) Long period earthquake

ground motion effects to improve structural resilience under varying seismic hazards.

Fig. 21 compares the Fixed Base and Soil-Structure Interaction (SSI) models under short- and long-period earthquakes, showing that the SSI model is more fragile in both cases. Fig. 21 (a) details the short-period response, where the SSI model exhibits significantly higher vulnerability, especially at higher risk levels. For instance, at a PGA of 0.2 g, the probability of Extensive damage increases from about 0.1 in the Fixed Base model to roughly 0.25 in the SSI model, highlighting the strong effect of soil-structure interaction in raising structural vulnerability during short-period seismic events.

Fig. 21 (b) compares model behavior under long-period earthquake excitation, showing increased fragility for both models compared to short-period cases. Differences between Fixed Base and SSI models are small for Slight and Moderate damage but grow significantly for severe damage states. At a PGA of 0.3 g, the Fixed Base model estimates a Complete failure probability of about 2.5, while the SSI model's probability nearly doubles to 5, highlighting how soil-structure interaction greatly increases vulnerability during intense long-period seismic events. Overall, the findings from Fig. 21 emphasize the necessity of incorporating SSI effects into seismic risk assessments, as neglecting these interactions can lead to underestimation of structural fragility, particularly for high damage states and long-period earthquake excitations. The increased vulnerability observed in the SSI model, particularly under long-period ground motions, is primarily associated with the elongation of the fundamental period resulting from soil structure interaction. The period shift places the structure closer to the peak region of spectral acceleration under long-period excitations, leading to higher seismic demands.

Additionally, the variation in effective damping plays a secondary role. Due to soil flexibility, the overall damping

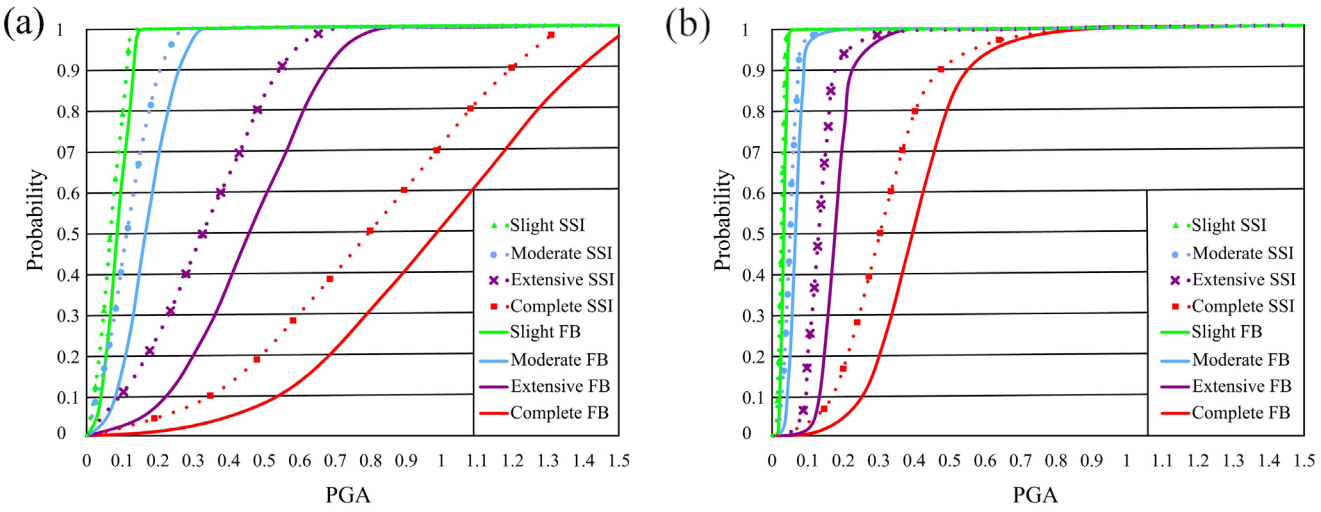

Fig. 21 The fragility curves at various damage states for SSI model and fixed-base under (a) Short period earthquake and (b) Long period earthquake

ratio of the system decreases slightly, which further reduces its ability to dissipate seismic input energy efficiently. This combined effect contributes to greater structural responses across all damage states. These insights are vital for improving the accuracy of seismic performance evaluations and informing design practices for earthquake-resilient structures.

Finally, Fig. 22 shows a general comparison between the two models, ShP (Short Period) and LP (Long Period), and a specific comparison between the two models, Fixed Base and SSI. Buildings exposed to long-period ground motions exhibit greater vulnerability to short-period earthquakes, especially when soil-structure interaction (SSI) is considered versus fixed-base (FB) conditions. Fig .23 shows median fragility values PGA levels with a 50% chance of exceeding damage states for four cases: long-period FB, short-period FB, long-period SSI, and short-period SSI. The chart highlights that models incorporating SSI consistently have lower PGA thresholds for damage, particularly under short-period events, indicating increased seismic vulnerability compared to fixed-base models.

Median seismic vulnerability values for the Fixed Base model under Long Period earthquakes are 0.033 g, 0.069 g, 0.18 g, and 0.4 g for Slight, Moderate, Extensive, and Complete damage levels, respectively, while under Short Period earthquakes, these values are higher: 0.09 g, 0.17 g, 0.46 g, and 0.99 g. This shows greater vulnerability under Long Period records in the Fixed Base model. For the SSI state, median values under Long Period earthquakes are 0.03 g, 0.05 g, 0.13 g, and 0.31 g, and under Short Period earthquakes, they are 0.075 g, 0.11 g, 0.32 g, and 0.8 g across the same damage levels. Comparing Fixed Base and SSI models indicates higher vulnerability in SSI state, with both models more susceptible to long-period than short-period earthquakes.

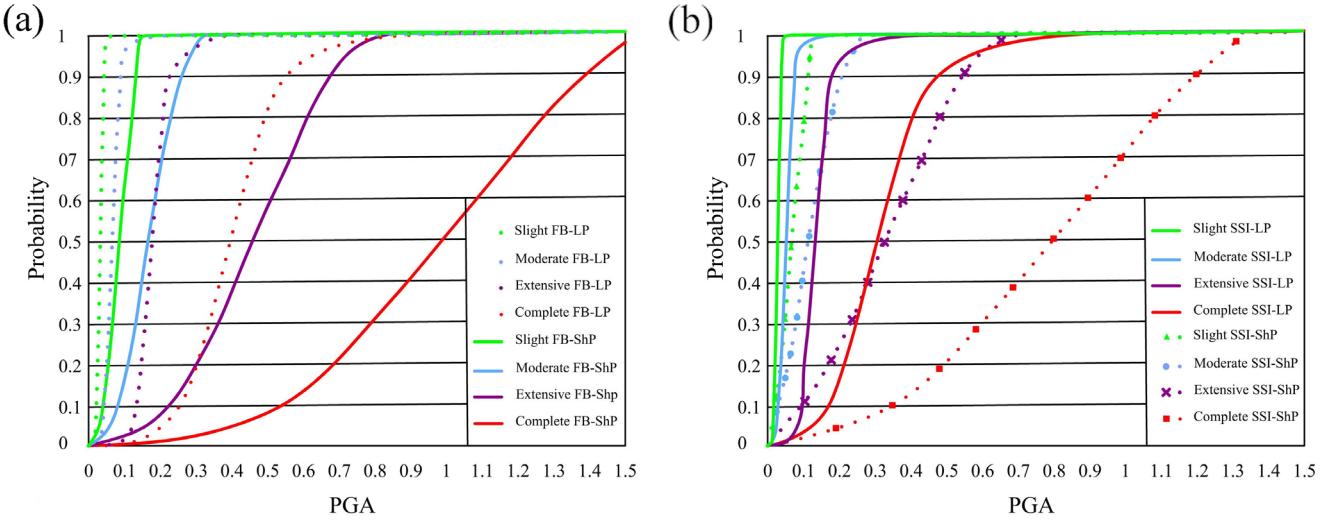

Fig. 22 Comparison of short-period and long-period earthquakes (a) Fixed Base model with Long Period and (b) SSI model with Short Period

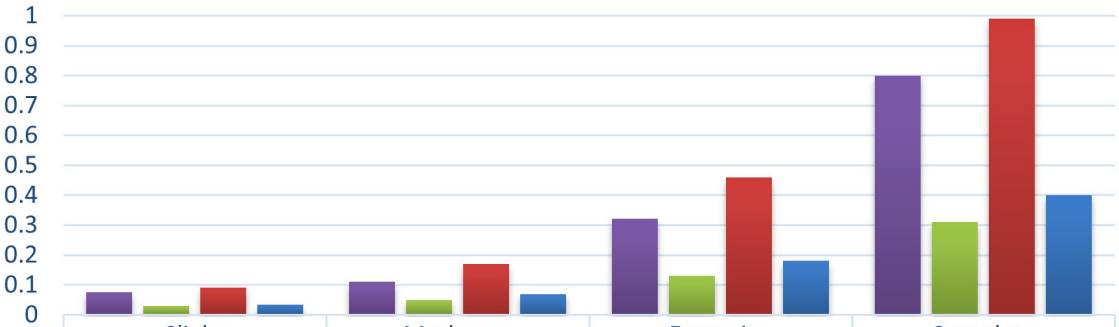

	Slight	Moderate	Extensive	Complete
Long Period For FB	0.033	0.069	0.18	0.4
Short Period For FB	0.09	0.17	0.46	0.99
Long Period For SSI	0.03	0.05	0.13	0.31
Short Period For SSI	0.075	0.11	0.32	0.8

Fig. 23 Median fragility of two Fixed Base and SSI models under Long Period and Short Period earthquakes in terms of g

12 Conclusions

This research investigated the probabilistic seismic performance of a 33-story reinforced concrete frame–tube building by developing fragility curves under both Fixed Base and Soil–Structure Interaction (SSI) conditions using nonlinear Incremental Dynamic Analysis with ground motions scaled from 0.1 g to 1.5 g. The results demonstrate that SSI significantly increases the probability of exceeding all damage states compared to the fixed-base condition, and structures reach the same damage level at lower PGA values when SSI is considered.

The main technical outcomes of this study can be summarized as follows:

1. Effect of Soil–Structure Interaction (SSI) on seismic fragility: SSI significantly increases the probability of exceeding all damage states. Structures subjected to SSI reach the same damage levels at lower PGA values, providing a more realistic assessment of seismic demand.
2. Higher sensitivity at advanced damage levels: The influence of SSI becomes more pronounced at higher damage states, where both vulnerability and variability of the seismic response increase, indicating that neglecting SSI may lead to non-conservative and unrealistic design predictions.
3. Engineering implications: The observed increase in displacement demands and period elongation, particularly under long-period ground motions, highlights the need for enhanced foundation stiffness, soil improvement measures, or the use of base isolation and energy-dissipation systems to mitigate adverse SSI effects.
4. Influence of ground motion period: A comparison between Short Period (ShP) and Long Period (LP) ground motions, as well as between Fixed Base (FB) and SSI models, reveals that buildings subjected to long-period excitations are generally more vulnerable to short-period earthquakes, particularly when SSI is considered.
5. Median fragility thresholds: Median PGA values corresponding to a 50% probability of exceeding damage states highlight that SSI models consistently have lower PGA thresholds for all damage levels compared to FB models. This indicates increased seismic vulnerability when soil–structure interaction is accounted for, especially under short-period events.
6. Site- and structure-specific limitations: The study is based on soil conditions from a specific site in Iran and a 33-story building; thus, quantitative results (including modal characteristics, damage probabilities, and vulnerability trends) may differ for softer soils or structures with different heights and stiffness. General trends, such as the impacts of SSI on period elongation, seismic response, and energy dissipation, are expected to be broadly applicable to other sites.
7. Recommendations for future research: Expanding the ground motion record set—by including near-fault, far-field, and pulse-like motions—would enhance the comprehensiveness and robustness of the fragility assessment, ensuring more generalizable and reliable seismic performance predictions.

References

[1] Kappos, A. J. "An overview of the development of the hybrid method for seismic vulnerability assessment of buildings", Structure and Infrastructure Engineering, 12(12), pp. 1573–1584, 2016. https://doi.org/10.1080/15732479.2016.1151448

[2] Silva, V. "Uncertainty and Correlation in Seismic Vulnerability Functions of Building Classes", Earthquake Spectra, 35(4), pp. 1515–1539, 2019. https://doi.org/10.1193/013018EQS031M

[3] Bradley, B. A. "A critical examination of seismic response uncertainty analysis in earthquake engineering", Earthquake Engineering & Structural Dynamics, 42(11), pp. 1717–1729, 2013. https://doi.org/10.1002/eqe.2331

[4] Soleimani, M., Pahlavan, H., Shamekhi Amiri, M., Dorrinia, N. "Evaluation of settlement and seismic response of high-rise buildings considering soil–structure interaction based on static loading results and continuum modeling", Amirkabir Journal of Civil Engineering, 57(7), pp. 1221–1244, 2025. https://doi.org/10.22060/ceej.2025.23821.8221

[5] Zamani, A. M., Pahlavan, H., Shamekhi Amiri, M., Rafee, F. "Probabilistic seismic assessment of RC tall regular buildings having special moment frames subjected to long-period earthquakes", Journal of Structural and Construction Engineering, 8(4), pp. 270–291, 2021. https://doi.org/10.22065/jsce.2021.281122.2421

[6] Naseri, A., Pahlavan, H. Ghodrati A. G. "Probabilistic seismic assessment of RC frame structures in North of Iran using fragility curves", Journal of Structural and Construction Engineering, 4(4), pp. 58–78, 2017. https://doi.org/10.22065/jsce.2017.78827.1095

[7] Pahlavan, H., Naseri, A., Einollahi, A. "Probabilistic Seismic Vulnerability assessment of RC Frame Structures Retrofitted with Steel Jacketing", Amirkabir Journal of Civil Engineering, 51(3), pp. 585–598, 2019. https://doi.org/10.22060/CEEJ.2018.13692.5459

[8] Pahlavan, H., Shayanfar, M., Ghodrati A. G., Pahlavan, M. "Probabilistic seismic vulnerability assessment of the structural deficiencies in Iranian in-filled RC frame structures", Journal of Vibroengineering, 17(5), pp. 2444–2454, 2015.

[9] Razmkhah, M. H., Shamekhi, A. M., Pahlavan, H. "Performance Seismic Assessment of Steel Frame Structures Having Torsional Irregularity Subjected to Mainshock-Aftershock", Journal of Structural and Construction Engineering, 8(8), pp. 249–265, 2021. https://doi.org/10.22065/jsce.2020.183112.1842

[10] Kouhestanian, H., Pahlavan, H., Shafaei, J., Shamekhi Amiri, M. "Probabilistic Seismic Assessment of RC Buildings Considering Soft and Extreme Soft Story irregularities Subjected to Main Shock-Aftershock Sequences", Amirkabir Journal of Civil Engineering, 53(2), pp. 457–478, 2021.

[11] Kouhestanian, H., Razmkhah, M. H., Shafaei, J., Pahlavan, H., Shamekhi, A. M. "Probabilistic Evaluation of Seismic Performance of Steel Buildings with Torsional Irregularities in Plan and Soft Story under Mainshock-Aftershock Sequence", Shock and Vibration, 2023(1), 9549121, 2023. https://doi.org/10.1155/2023/9549121

[12] Basefat, A. Z. M., Pahlavan, H., Shamekhi Amiri, M., Shafaei, J. "Investigating the influence of near-field excitations on the seismic performance of special tall RC moment frame structures", Bulletin of Earthquake Science and Engineering, 12(2), pp. 27–40, 2025. https://doi.org/10.48303/bese.2024.2033212.1181

[13] Koosha, A., Pahlavan, H. Shamekhi A. M. "Probabilistic Seismic Performance Assessment of Tall RC Frame-Core Buildings Having Hybrid Coupled Shear Walls Considering Long-Period Earthquakes", The Structural Design of Tall and Special Buildings, 34(11), e70053, 2025. https://doi.org/10.1002/tal.70053

[14] Zarif Moghadam Basefat, A., Pahlavan, H., Shafaei, J. "Probabilistic Seismic Performance Assessment of Tall RC Special Moment-resisting Frame Buildings Equipped with Buckling-restrained Braces under Near-field Excitations", Periodica Polytechnica Civil Engineering, 68(2), pp. 524–542, 2024. https://doi.org/10.3311/PPci.20914

[15] Pahlavan, H., Zarif M. B. A., Shamekhi A. M., Namiranian, P. "Probabilistic seismic performance assessment of tall buildings having special RC moment frames equipped with buckling restrained braces (BRB)", Journal of Structural and Construction Engineering, 8(1), pp. 230–250, 2021. https://doi.org/10.22065/jsce.2020.198620.1929

[16] Zarif M. B. A., Pahlavan, H., Shamekhi, A. M., Shafaei, J. "Probabilistic seismic performance assessment of tall RC buildings equipped with energy dissipator devices", Structures, 75, 108834, 2025. https://doi.org/10.1016/j.istruc.2025.108834

[17] Mylonakis, G., Gazetas, G. "Seismic soil–structure interaction: beneficial or detrimental?", Journal of Earthquake Engineering, 4(3), pp. 277–301, 2000. https://doi.org/10.1080/13632460009350372

[18] Karatzetzou, A., Pitilakis, D. "Reduction factors to evaluate acceleration demand of soil–foundation–structure systems", Soil Dynamics and Earthquake Engineering, 109, pp. 199–208, 2018. https://doi.org/10.1016/j.soildyn.2018.03.017

[19] Pitilakis, D., Moderessi-Farahmand-Razavi, A., Clouteau, D. "Equivalent-Linear Dynamic Impedance Functions of Surface Foundations", Journal of Geotechnical and Geoenvironmental Engineering, 139(7), pp. 1130–1139, 2013. https://doi.org/10.1061/(ASCE)GT.1943-5606.0000829

[20] Gonzalez, J. M., Barbat, A. H., Vargas-Alzate, Y. F., Rastellini, F., Ramirez, J., Escudero, C., Pujades, L. G. "Advanced nonlinear soil–structure interaction model for the seismic analysis of safety-related nuclear structures", Bulletin of Earthquake Engineering, 22(15), pp. 7465–7488, 2024. https://doi.org/10.1007/s10518-024-02055-z

[21] Mortezaei, A. "Plastic hinge length of RC columns considering soil–structure interaction", Earthquakes and Structures, 5(6), pp. 679–696, 2013. https://doi.org/10.12989/eas.2013.5.6.679

[22] Yepes-Estrada, C., Silva, V., Rossetto, T., D'Ayala, D., Ioannou, I., Meslem, A., Crowley, H. "The global earthquake model physical vulnerability database", Earthquake Spectra, 32(4), pp. 2567–2585, 2016.
https://doi.org/10.1193/011816EQS015DP

[23] Midas "Midas Civil (version 2022)", [computer program] Available at: https://www.midasoft.com/product/midascivil/

[24] Fatahi, B., Huang, B., Yeganeg, N., Terzaghi, S., Banerjee, S. "Three-Dimensional Simulation of Seismic Slope–Foundation–Structure Interaction for Buildings Near Shallow Slopes", International Journal of Geomechanics, 20(1), 04019140, 2020.
https://doi.org/10.1061/(ASCE)GM.1943-5622.0001529

[25] Amorosi, A., Boldini, D., Di Lernia, A. "Seismic ground response at Lotung: Hysteretic elasto-plastic-based 3D analyses", Soil Dynamics and Earthquake Engineering, 85, pp. 44–61, 2016.
https://doi.org/10.1016/j.soildyn.2016.03.001

[26] ASTM "ASTM D1586/D1586M-18e1 Standard Test Method for Standard Penetration Test (SPT) and Split-Barrel Sampling of Soils", ASTM International, West Conshohocken, PA, USA, 2018.
https://doi.org/10.1520/D1586_D1586M-18E01

[27] Ahmad, N., Masoudi, M., Salawdeh, S. "Cyclic response and modelling of special moment resisting beams exhibiting fixed-end rotation", Bulletin of Earthquake Engineering, 19(1), pp. 203–240, 2021.
https://doi.org/10.1007/s10518-020-00987-w

[28] Roy, T., Saito, T., Matsagar, V. "Multihazard framework for investigating high-rise base-isolated buildings under earthquakes and long-duration winds", Earthquake Engineering & Structural Dynamic, 50(5), pp.1334–1357, 2021.
https://doi.org/10.1002/eqe.3401

[29] Shamsi, M., Ghanbari, A. "Nonlinear dynamic analysis of Qom Monorail Bridge considering Soil–Pile–Bridge–Train Interaction", Transportation Geotechnics, 22, 100309, 2020.
https://doi.org/10.1016/j.trgeo.2019.100309

[30] ASTM "ASTM D1143/D1143M-20e1 Standard Test Methods for Deep Foundation Elements Under Static Axial Compressive Load", ASTM International, West Conshohocken, PA, USA, 2020.
https://doi.org/10.1520/D1143_D1143M-20E01

[31] Bian, X., Chen, J., Chen, X., Xu, Z. "Reliability-Based Design of Driven Piles Considering Setup Effects", Applied Sciences, 11(18), 8609, 2021.
https://doi.org/10.3390/app11188609

[32] Thomsen IV, J. H., Wallace, J. W. "Displacement-Based Design of Slender Reinforced Concrete Structural Walls - Experimental Verification", Journal of Structural Engineering, 130(4), pp. 618–630, 2004.
https://doi.org/10.1061/(ASCE)0733-9445(2004)130:4(618)

[33] Mander, J. B., Priestley, M. J. N., Park, R. "Theoretical Stress–Strain Model For Confined Concrete", Journal of Structural Engineering, 114(8), pp. 1804–1826, 1988.

[34] Rizzitano, S., Cascone, E., Biondi, G. "Coupling of topographic and stratigraphic effects on seismic response of slopes through 2D linear and equivalent linear analyses", Soil Dynamics and Earthquake Engineering, 67, pp. 66–84, 2014.
https://doi.org/10.1016/j.soildyn.2014.09.003

[35] Rayhani, M. H., El Naggar, M. H. "Numerical Modeling of Seismic Response of Rigid Foundation on Soft Soil", International Journal of Geomechanics, 8(6), pp. 336–346, 2008.
https://doi.org/10.1061/(ASCE)1532-3641(2008)8:6(336)

[36] Manna, B., Baidya, D. K. "Vertical Vibration of Full-Scale Pile–Analytical and Experimental Study", Journal of Geotechnical and Geoenvironmental Engineering, 135(10), pp. 1452–1461, 2009.
https://doi.org/10.1061/(ASCE)GT.1943-5606.0000110

[37] Nguyen, Q. V., Fatahi, B., Hokmabadi, A. S. "Influence of Size and Load-Bearing Mechanism of Piles on Seismic Performance of Buildings Considering Soil–Pile–Structure Interaction", International Journal of Geomechanics, 17(7), 04017007, 2017.
https://doi.org/10.1061/(ASCE)GM.1943-5622.0000869

[38] Fatahi, B., Nguyen, Q. V., Xu, R., Sun, W. "Three-Dimensional Response of Neighboring Buildings Sitting on Pile Foundations to Seismic Pounding", International Journal of Geomechanics, 18(4), 04018007, 2018.
https://doi.org/10.1061/(ASCE)GM.1943-5622.0001093

[39] Applied Technology Council "Quantification of Building Seismic Performance Factors", [online] Federal Emergency Management Agency (FEMA), Washington, DC, USA, Rep. FEMA P695, 2009. Available at: https://nehrpsearch.nist.gov/static/files/FEMA/fema_p695.pdf [Accessed: 13 October 2025]

[40] American Society of Civil Engineering "Minimum Design Loads and Associated Criteria for Buildings and Other Structures (ASCE/SEI 7-10)", Structural Engineering Institute (SEI), Reston, VA, USA, 2010.

[41] Seismosoft "SeismoStruct (v2024)", [computer program] Available at: https://seismosoft.com/product/seismostruct/

[42] Dorrinia, N., Pahlavan, H., Amiri, M. S., Sirjani, M. "Seismic Assessment of RC Tall Core–Frame Buildings Considering Soil–Structure Interaction (SSI)", Iranian Journal of Science and Technology, Transactions of Civil Engineering, 2025.
https://doi.org/10.1007/s40996-025-01837-y

[43] Vamvatsikos, D., Cornell, C. A. "Incremental dynamic analysis", Earthquake Engineering & Structural Dynamics, 31(3), pp. 491–514, 2002.
https://doi.org/10.1002/eqe.141

[44] Porter, K. A., Kennedy, R., Bachman, R. "Creating Fragility Functions for Performance-Based Earthquake Engineering", Earthquake Spectra, 23(2), pp. 471–489, 2007.

[45] Chopra, A. K. "Dynamics of Structures: Theory and Applications to Earthquake Engineering", Pearson, 2011. ISBN 978-0132858038